REPORTS

PLANETARY SCIENCE

Low-altitude magnetic field measurements by MESSENGER reveal Mercury's ancient crustal field

Catherine L. Johnson,[1,2]* Roger J. Phillips,[3] Michael E. Purucker,[4] Brian J. Anderson,[5] Paul K. Byrne,[6,13] Brett W. Denevi,[5] Joshua M. Feinberg,[7] Steven A. Hauck II,[8] James W. Head III,[9] Haje Korth,[5] Peter B. James,[10] Erwan Mazarico,[4] Gregory A. Neumann,[4] Lydia C. Philpott,[1] Matthew A. Siegler,[2,11] Nikolai A. Tsyganenko,[12] Sean C. Solomon[10,13]

Magnetized rocks can record the history of the magnetic field of a planet, a key constraint for understanding its evolution. From orbital vector magnetic field measurements of Mercury taken by the MErcury Surface, Space ENvironment, GEochemistry, and Ranging (MESSENGER) spacecraft at altitudes below 150 kilometers, we have detected remanent magnetization in Mercury's crust. We infer a lower bound on the average age of magnetization of 3.7 to 3.9 billion years. Our findings indicate that a global magnetic field driven by dynamo processes in the fluid outer core operated early in Mercury's history. Ancient field strengths that range from those similar to Mercury's present dipole field to Earth-like values are consistent with the magnetic field observations and with the low iron content of Mercury's crust inferred from MESSENGER elemental composition data.

Mercury is the only inner solar system body other than Earth that currently possesses a global magnetic field generated by a dynamo in a fluid metallic outer core (*1*, *2*). Mercury's field is dipolar, weak (surface field strength ~1% that of Earth's), axially symmetric, and equatorially asymmetric (*3*–*5*). These attributes may indicate an intrinsic north-south asymmetry in the dynamo (*6*). The basic characteristics of the magnetic field have persisted for at least the past ~40 years, the duration of the era of spacecraft exploration of Mercury (*7*), but whether a field was present over longer time scales has been unknown. We show here that Mercury's core dynamo field was also present early in the planet's history, providing critical information on Mercury's interior thermal and dynamic evolution.

[1]Department of Earth, Ocean and Atmospheric Sciences, University of British Columbia, Vancouver, BC, V6T 1Z4, Canada. [2]Planetary Science Institute, Tucson, AZ 85719, USA. [3]Planetary Science Directorate, Southwest Research Institute, Boulder, CO 80302, USA. [4]NASA Goddard Space Flight Center, Greenbelt, MD 20771, USA. [5]The Johns Hopkins University Applied Physics Laboratory, Laurel, MD 20723, USA. [6]Lunar and Planetary Institute, Houston, TX 77058, USA. [7]Institute for Rock Magnetism, Department of Earth Sciences, University of Minnesota, Minneapolis, MN, 55455, USA. [8]Department of Earth, Environmental, and Planetary Sciences, Case Western Reserve University, Cleveland, OH, 44106, USA. [9]Department of Earth, Environmental and Planetary Sciences, Brown University, Providence, RI 02912, USA. [10]Lamont-Doherty Earth Observatory, Columbia University, Palisades, NY 10964, USA. [11]Department of Earth Sciences, Southern Methodist University, Dallas, TX 75205, USA. [12]Institute and Faculty of Physics, Saint Petersburg State University, Saint Petersburg, Russia. [13]Department of Terrestrial Magnetism, Carnegie Institution of Washington, Washington, DC 20015, USA.
*Corresponding author. E-mail: cjohnson@eos.ubc.ca

Magnetized rocks and the fields that result from them are key records of a planet's magnetic field history. Igneous rocks that cool in the presence of an ambient magnetic field can acquire a permanent or remanent magnetization determined by their mineralogy and by the strength and geometry of the magnetizing field. Such magnetization can be altered by subsequent tectonic activity, reheating, burial, shock, or chemical reactions. Lateral variations in the strength or direction of magnetization, or in the thickness or depth of the magnetized layer, give rise to magnetic anomalies that may be detected on or above the surface. Detection of these anomalies depends on the strength and horizontal scale of the magnetization contrasts and on the distance of the observation platform from the magnetized source.

Orbital observations of Mercury's magnetic field by the Magnetometer on the MErcury Surface, Space ENvironment, GEochemistry, and Ranging (MESSENGER) spacecraft have been made from March 2011 to April 2015. MESSENGER's orbit was highly eccentric, and until 2014, minimum (periapsis) altitudes were 200 to 500 km. Fields resulting from remanent crustal magnetization have not been detected in these observations, a result suggesting that remanent magnetization is weak to nonexistent, or coherent only over spatial scales less than a few hundred kilometers.

Magnetic field measurements were obtained by MESSENGER at spacecraft altitudes less than 200 km starting in April 2014. Mercury's offset-axial dipole core field, and fields from the magnetopause and magnetotail current systems and other external sources, dominate the observations (*4*, *5*, *8*, *9*). We estimated these contributions for each orbit, using magnetospheric models developed with MESSENGER data (*5*, *9*), and subtracted them from the vector magnetic field measurements. The remaining signals have magnitudes of a few tens of nT and wavelengths of several hundred to ~1500 km and change substantially from one orbit to the next. They originate mainly from processes operating above the surface of Mercury (*5*, *9*, *10*). These fields mask any smaller-amplitude, shorter-wavelength signals from the planet's interior. We estimated the long-wavelength signals empirically on an orbit-by-orbit basis and removed them by the application of a high-pass filter (*10*) tuned to best separate the short- and long-wavelength signals (Fig. 1).

Typically, the high-pass filtered (HPF) data show either no signals or signals that are correlated with increased variability in the total field at frequencies above 1 Hz. The latter—e.g., those during the time period 1200 to 1260 s in Fig. 1, B and C—are not of internal origin. However, for some orbits, the HPF data show smoothly varying signals that have amplitudes more than three times that of the high-frequency variability. These signals are found close to periapsis (Fig. 1D) and are typically observed on multiple successive orbits (e.g., Fig. 1 and figs. S1 to S4).

We have detected radial (ΔB_r) and colatitudinal (north-south, ΔB_θ) HPF signals with these characteristics over the two regions where MESSENGER periapsis altitudes were lowest (~25 km) in 2014: the Suisei Planitia region (Fig. 2) and a region south of the lobate scarp Carnegie Rupes (*10*). We also detected weaker signals, less than 3 nT in amplitude, over a third region near ~170°E, at times close to periapsis and altitudes of ~95 to ~130 km in 2014. Clear detections have been made on only nightside or dawn-dusk tracks because of lower high-frequency variability in external fields than on the dayside.

Coherent signals across the Suisei Planitia region obtained in orbits from September 2014 display peak amplitudes of ~12 nT at spacecraft altitudes of 27 km, north of Shakespeare basin (Fig. 2A). The dominant wavelength of the signals is ~320 km, but shorter-wavelength signals are also observed. We verified that these results are insensitive to the precise choice of the HPF characteristics, to first order (*10*) (fig. S5), and that the magnetospheric activity index (*11*) was not unusually high during most orbits (*10*) (fig. S6).

The eastern extent of the signals is well constrained by the MESSENGER data, with no signals observed at ~60°N, east of Kosho crater (~220°E), even though periapsis altitudes were below 30 km eastward to 240°E. The westernmost extent (Fig. 2A) corresponds to an orbit-correction maneuver (OCM) that raised periapsis altitude from 25 to 94 km. No signals were detected on orbits immediately following the OCM (fig. S4); this altitude dependence suggests that the source of the fields is internal. Furthermore, the dominant wavelengths of the signals observed at the lowest spacecraft altitudes are consistent with source depth estimates of 7 to 45 km, suggesting magnetized rocks as the source of the observed fields rather than contributions from

the core (*10*). Confirmation of an internal origin is provided by the weaker signals observed at altitudes of 60 to 100 km (fig. S7A) and the absence of signals at ~150 km altitude. These observations are consistent with the upward attenuation of signals from the lowest altitudes predicted for an internal source (*10*) (fig. S7B). Finally, signals very similar in character to those in Fig. 2A were observed over the region in March 2015, at the same local times as September 2014 and at spacecraft altitudes of 14 to 40 km. Larger amplitudes were observed within ~5° latitude of periapsis (~59°N), reflecting the 10-km-lower periapsis altitude. Low-altitude observations from March extend to the western edge of the region and show signals west of Verdi crater, in particular over the adjacent volcanic smooth plains. All data obtained at spacecraft altitudes below 60 km are shown in Fig. 2B.

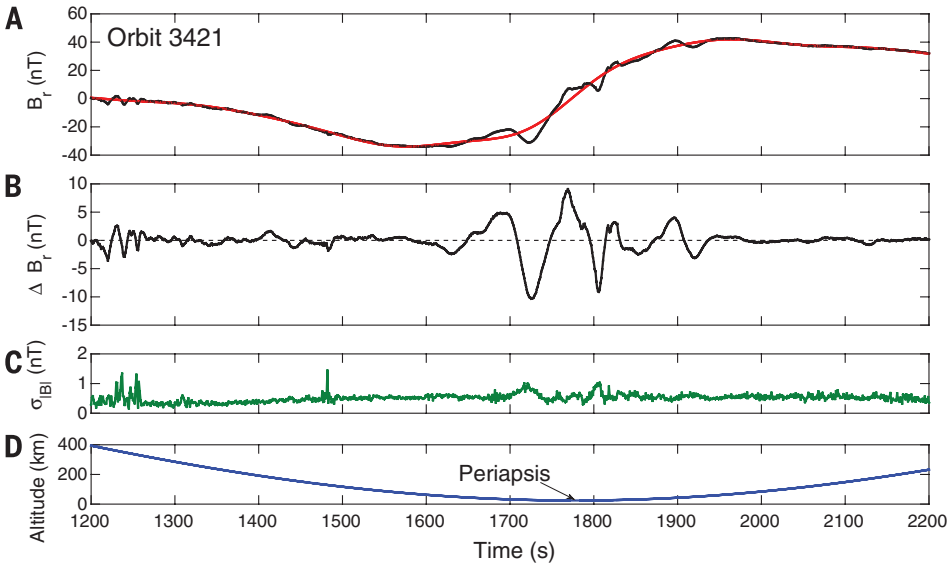

Fig. 1. Magnetic field observations from 8 September 2014 (orbit 3421). (**A**) Radial component of the field, B_r (black), in the Mercury body-fixed frame (*10*) after subtraction of the modeled magnetopause, magnetotail, and offset axial dipole fields, and the low-pass filtered signal (red). (**B**) HPF signal, ΔB_r. (**C**) High-frequency (>1 Hz) variability in the total field, $\sigma_{|B|}$, a measure of the external field noise remaining in the HPF signals. (**D**) Spacecraft altitude. Periapsis altitude was 25 km. 100 s corresponds to a horizontal scale of ~385 km at periapsis. The orbit track is labeled on Fig. 2A.

The HPF signals are seen over, but are not restricted to, regions of lower topography (Fig. 2A and fig S8). In the Suisei Planitia region, signals are seen over regions of both smooth plains and older intercrater plains (Fig. 2B) (*12*, *13*). The largest-amplitude ΔB_r values are spatially associated with smooth plains (Fig. 2B) (*10*). There are no obvious features associated with impact craters in the Suisei region, and no clear signals at the edge of the Borealis basin (fig. S8) have yet been observed, although there are weak signals over the eastern interior of the basin. Contractional structures CS1 and CS2 (Fig. 2A) indicate local association of the signals with tectonic features, but many structures in the region (*14*), such as CS3 and CS4, have no associated ΔB_r signals (Fig. 2A). Similarly, no coherent signals have been seen across Carnegie Rupes (fig. S8). Our observations are consistent with sources at depth that may include a combination of magnetized intrusive material and magnetization contrasts across deep-seated crustal structures (e.g., faults). Features associated with mapped tectonic structures (e.g., the local maximum in ΔB_r over CS1) may reflect sources at shallower depths.

Constraining the time of acquisition of magnetic remanence is difficult because the signals do not correlate with regions of distinctive

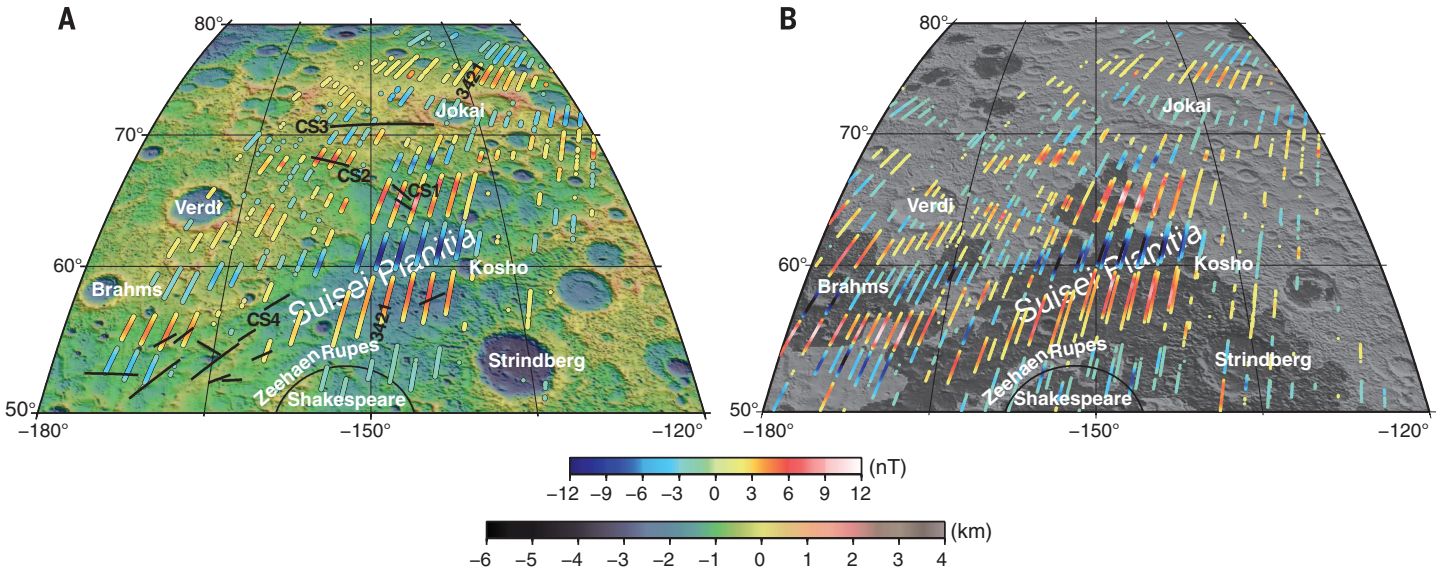

Fig. 2. HPF radial magnetic field, ΔB_r, over Suisei Planitia. The HPF signals shown satisfy $|\Delta B_r| \geq 1$ nT and $|\Delta B_r|/\sigma_{|B|} \geq 3$. Underlying image is of topography derived from Mercury Laser Altimeter measurements (Mollweide projection). Color bars give ΔB_r (nT) and topography (km). 1° of latitude on Mercury corresponds to 43 km. (**A**) Orbits 3411 to 3433 (from September 2014), excluding orbit 3424 (high magnetospheric activity). The time interval between successive orbits is 8 hours. Orbit 3421 (Fig. 1) is labeled. Periapsis local times were 06:00 to 08:30 hours. Spacecraft altitudes were 25 to 60 km. The Shakespeare basin and contractional structures at least 50 km in length, with a strike making an angle greater than 45° to the orbit track, are shown in black. CS1 to CS4 are contractional structures. (**B**) Orbits 3411 to 3433 (as in Fig. 2A) and orbits 3928 to 3940 (from March 2015) at spacecraft altitudes of 14 to 40 km. Periapsis local times were 06:00 to 08:30 hours for all orbits. Underlying image shows the smooth plains in dark gray (*12*) and intercrater plains in light gray. The observations from March 2015 show the repeatability of the signals observed in Fig. 2A and higher amplitudes associated with the lower spacecraft altitudes (peak amplitudes of 20 nT observed at 15 km altitude).

surface ages. However, the presence of signals over relatively large areas (Fig. 2 and fig. S8) that encompass multiple geologic units, together with the observation that the largest-amplitude ΔB_r values occur over the smooth plains, suggests that the smooth plains, the youngest major volcanic deposits on Mercury emplaced 3.7 to 3.9 billion years ago (Ga) (*12*, *15*), provide a lower bound on the average age of magnetization. An average age substantially less than this figure would require processes that operated over large regions after smooth plains emplacement yet left no surficial expression. Such processes could include pervasive intrusions at depth that remained below the Curie temperature of the magnetic carrier mineral(s) after cooling; reheating and subsequent cooling of older intrusive material; subsurface structural deformation of previously magnetized material; or some combination of the two. Although later acquisition of remanence may have occurred locally (e.g., during cooling of impact melt), the association of crustal remanence with diverse terrains suggests that much of the magnetization was acquired in an internal field before 3.7 to 3.9 Ga. The dominance of ΔB_r and ΔB_θ signals across groups of orbits, together with the ΔB_ϕ signals on orbits immediately to the east and west of these groups (*10*) (fig. S9), are consistent with a magnetization that is primarily in the north-south plane and is associated with features that are limited in their east-west extent. The simplest geometry for the field in which such a remanence was acquired is one that, like the current field, was symmetric about the planet's rotation axis (*10*).

The peak strength of the signals over Suisei Planitia provides a lower bound on the magnetization (M) within a layer of a given thickness (*10*). For thicknesses of 4 to 40 km, M values are 0.1 to 0.02 Am^{-1}, respectively, comparable to those inferred for the Moon (*16*). For thermoremanence, M reflects the combined effects of the strength of the magnetizing field ($B_{ancient}$) and the bulk magnetic properties of the crust, given by its thermoremanent susceptibility (χ_{TRM}). Values for $B_{ancient}$ and χ_{TRM} were calculated from the relation $M = \chi_{TRM} B_{ancient} / \mu_0$, where μ_0 is the magnetic permeability of free space, for layer thicknesses ranging from 1 to 100 km (*17*). The thermoremanent susceptibility of Mercury's crust is unknown, because it depends on the magnetic minerals present and on their relative volumetric abundances. The chemically reduced characteristics of Mercury's surface materials (*18*) suggest that iron metal, iron alloys, and iron sulfides are possible magnetic carriers. Given Mercury's low oxygen fugacity (*19*), the paramagnetic iron sulfide troilite is likely to be a more stable mineral than the ferromagnetic pyrrhotite. However, because knowledge of the petrology of Mercury's interior is limited, we evaluated the plausibility of pyrrhotite or a mineral with similar magnetic characteristics (χ_{TRM} and Curie temperature, T_c) as a potential magnetic phase. Susceptibilities for pyrrhotite, iron metal, and high-iron (EH) and low-iron (EL) enstatite chondrites were scaled for volume fractions of the magnetic carrier consistent with the 1.5 to 2 weight percent average iron content inferred from MESSENGER x-ray fluorescence observations (*10*, *20*, *21*). The results (Fig. 3) indicate that for magnetic layer thicknesses of 25 km, consistent with the average source depth and mean crustal thickness (Fig. 4) in the region, EH values for χ_{TRM} require surface field strengths about twice those of the present-day value in the Suisei region (~300 nT). The required field scales inversely with χ_{TRM} and with layer thickness. In particular, EL values for χ_{TRM} require a ~4500-nT field for a 25-km-thick layer.

The field values implied by the magnetic mineralogies for a given layer thickness (Fig. 3) are minima for two reasons. First, they are inferred from M, which is a lower bound on the magnetization, and second, they are derived under the assumption that all the iron is partitioned into magnetic phases. Earth-like fields (~50,000 nT) are permissible if χ_{TRM} is ~6×10^{-4} for a 25-km-thick layer, compatible with 0.1 to 5% of the iron partitioning into magnetic phases. Field strengths weaker than those today are unlikely, on the basis of the values of susceptibility required. Thus, ancient surface field strengths that lie between values comparable to those from Mercury's current dynamo and Earth-like values are most likely given the possible magnetic minerals in Mercury's crust.

We considered two alternative interpretations of the magnetization: first, that it reflects an

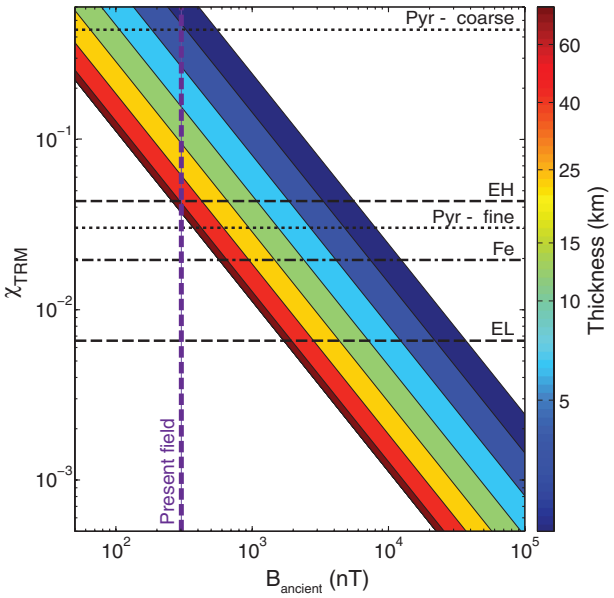

Fig. 3. Mercury's ancient field strength and magnetic mineralogy. Magnetic susceptibility (χ_{TRM}) and magnetizing field strength ($B_{ancient}$) required to produce the observed peak HPF magnetic field strength over Suisei Planitia. Susceptibilities (*10*) for pyrrhotite for grain sizes ranging from 5 to 250 μm (black dotted lines), multidomain iron (black dashed-dot line), and EH and EL enstatite chondrites (black dashed lines) are shown. The values are scaled for volume fractions of the magnetic carrier consistent with the average iron content inferred from MESSENGER observations. The surface field strength for the present internal dipole (vertical dashed line) is that for the average magnetic latitude of the region (46° N).

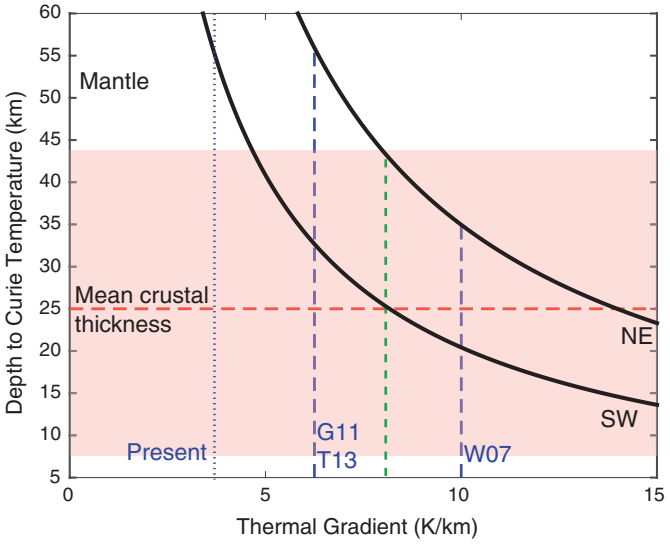

Fig. 4. Depth to the Curie temperature versus thermal gradient on Mercury. Depth to the Curie temperature (T_c = 325°C) for pyrrhotite across the Suisei Planitia region (black lines) as a function of thermal gradient. The two lines reflect the range in depths associated with a decrease in the mean surface temperature from the southwest [closer to the hot pole (*10*) at 0°N, 180°E] to the northeast of the region (fig. S11A). Curves for magnetic minerals with higher T_c lie to right of those shown here (fig. S11B). Blue dashed lines denote the range in thermal gradients at 4 Ga permitted by thermal evolution models W07 (*26*), G11 (*27*), and T13 (*28*); the blue dotted line is the average present value from thermal models (*26*–*28*). The mean crustal thickness (red dashed line) and the range in the mean value (red shaded region) in the region are shown (*22*–*24*). A thermal gradient less than that shown by the green dashed line implies that the uppermost mantle is cooler than the Curie temperature.

induced magnetization in the present field and, second, that it could be a viscous remanent magnetization (VRM) acquired during prolonged exposure of the magnetic minerals to the planetary field and hence reflecting an unknown, but younger, age than that of the smooth plains. Although both of these physical processes are likely to operate, induced magnetizations cannot fully explain the observed HPF field strengths, and the net effect of VRM will be that our estimates of ancient field strength are lower bounds (*10*).

Within the range of uncertainty of crustal thickness (*22*–*24*) and magnetized layer source depths (*10*), most or all of the magnetization could reside within Mercury's crust (Fig. 4). We investigated whether such a scenario is consistent with thermal evolution models, given magnetizations acquired at ~4 Ga. We estimated the depth to T_c for a range of thermal gradients (Fig. 4). The Curie temperature was taken to be 325°C (that of pyrrhotite) as a conservatively low value for our calculations, and we used the maximum average daily surface temperature predicted for a range of Mercury's orbital eccentricities from 0 to 0.4 (*10*, *25*). The results indicate that even for high thermal gradients at 4 Ga (*26*) the depth to T_c in the Suisei Planitia region is at least 20 km. For thermal gradients less than 8 K/km and upper limits on the crustal thickness in the region, the entire crust remains below T_c. These results imply that acquisition and subsequent preservation of an ancient crustal remanence by magnetic carriers with T_c values of at least 325°C are consistent with thermal models (*10*, *26*–*28*), and for carriers with higher T_c some remanence may be carried by upper mantle material. Such a conclusion is predicated on the assumption that the surface temperature pole locations have remained stationary in a body-fixed coordinate system since the time that the remanent magnetization was acquired (*10*). The symmetry of the ancient field with respect to the present rotation axis supports such a presumption by suggesting that, since that epoch, there has been no substantial reorientation of the crust ("true polar wander") with respect to the planet's axis of greatest moment of inertia.

The simplest interpretation of the results presented here is that a core dynamo was present early in Mercury's history. If the dynamo was thermochemically driven [e.g., (*6*, *29*)], this finding provides a strong constraint on models for the thermal evolution of Mercury's interior. In particular, the existence of a core dynamo at the time of smooth plains emplacement presents a new challenge to such models. An early core dynamo can be driven by superadiabatic cooling of the liquid core, but in typical thermal history models this phase has ended by 3.9 Ga. A later dynamo can be driven by the combined effects of cooling and compositional convection associated with formation of a solid inner core (*26*–*28*), but in most thermal history models inner core formation does not start until well after 3.7 Ga. Further progress in understanding the record of Mercury's ancient field can also be made with improved petrological constraints on crustal compositions [e.g., (*30*)], information on the candidate magnetic mineralogies implied, and knowledge of their magnetic properties.

REFERENCES AND NOTES

1. N. F. Ness, K. W. Behannon, R. P. Lepping, Y. C. Whang, K. H. Schatten, *Science* **185**, 151–160 (1974).
2. B. J. Anderson *et al.*, *Science* **321**, 82–85 (2008).
3. B. J. Anderson *et al.*, *Science* **333**, 1859–1862 (2011).
4. B. J. Anderson *et al.*, *J. Geophys. Res.* **117** (E12), E00L12 (2012).
5. C. L. Johnson *et al.*, *J. Geophys. Res.* **117** (E12), E00L14 (2012).
6. H. Cao *et al.*, *Geophys. Res. Lett.* **41**, 4127–4134 (2014).
7. L. C. Philpott *et al.*, *Geophys. Res. Lett.* **41**, 6627–6634 (2014).
8. B. J. Anderson *et al.*, *Geophys. Res. Lett.* **41**, 7444–7452 (2014).
9. H. Korth *et al.*, Modular model for Mercury's magnetospheric magnetic field confined within the average observed magnetopause. JGR Space Physics, doi10.1002/2015JA021022 (2015).
10. Materials and methods are available as supplementary materials on *Science* Online.
11. B. J. Anderson, C. L. Johnson, H. Korth, *Geochem. Geophys. Geosyst.* **14**, 3875–3886 (2013).
12. B. W. Denevi *et al.*, *J. Geophys. Res. Planets* **118**, 891–907 (2013).
13. J. L. Whitten, J. W. Head, B. W. Denevi, S. C. Solomon, *Icarus* **241**, 97–113 (2014).
14. P. K. Byrne *et al.*, *Nat. Geosci.* **7**, 301–307 (2014).
15. S. Marchi *et al.*, *Nature* **499**, 59–61 (2013).
16. M. E. Purucker, J. B. Nicholas, *J. Geophys. Res.* **115** (E12), E12007 (2010).
17. M. A. Wieczorek, B. P. Weiss, S. T. Stewart, *Science* **335**, 1212–1215 (2012).
18. L. R. Nittler *et al.*, *Science* **333**, 1847–1850 (2011).
19. F. M. McCubbin, M. A. Riner, K. E. Vander Kaaden, L. K. Burkemper, *Geophys. Res. Lett.* **39**, L09202 (2012).
20. L. G. Evans *et al.*, *J. Geophys. Res.* **117** (E12), E00L07 (2012).
21. S. Z. Weider, L. R. Nittler, R. D. Starr, T. J. McCoy, S. C. Solomon, *Icarus* **235**, 170–186 (2014).
22. E. Mazarico *et al.*, *J. Geophys. Res. Planets* **119**, 2417–2436 (2014).
23. P. B. James, M. T. Zuber, R. J. Phillips, S. C. Solomon, *J. Geophys. Res. Planets* **120**, 287–310 (2015).
24. S. Padovan, M. A. Wieczorek, J.-L. Margot, N. Tosi, S. C. Solomon, *Geophys. Res. Lett.* **42**, 1029–1038 (2015).
25. A. C. M. Correia, J. Laskar, *Icarus* **201**, 1–11 (2009).
26. J.-P. Williams, O. Aharonson, F. Nimmo, *Geophys. Res. Lett.* **34**, L21201 (2007).
27. M. Grott, D. Breuer, M. Laneuville, *Earth Planet. Sci. Lett.* **307**, 135–146 (2011).
28. N. Tosi, M. Grott, A.-C. Plesa, D. Breuer, *J. Geophys. Res. Planets* **118**, 2474–2487 (2013).
29. S. Stanley, G. A. Glatzmaier, *Space Sci. Rev.* **152**, 617–649 (2010).
30. K. E. Vander Kaaden, F. M. McCubbin, *J. Geophys. Res. Planets* **120**, 195–209 (2015).

ACKNOWLEDGMENTS

We thank the MESSENGER operations and engineering teams for enabling the low-altitude observations reported here. We are also grateful for the contributions of our friend and colleague M. H. Acuña whose expertise was critical to the Magnetometer development. The MESSENGER mission is supported by the NASA Discovery Program and the MESSENGER Participating Scientist Program. C.L.J. and L.C.P. also acknowledge support from the Natural Sciences and Engineering Research Council of Canada. Data from the MESSENGER mission are archived with the NASA Planetary Data System. We thank three reviewers for thoughtful comments that improved the manuscript.

SUPPLEMENTARY MATERIALS

www.sciencemag.org/content/348/6237/892/suppl/DC1
Supplementary Text
Figs. S1 to S11
Tables S1 and S2
References (31–53)

7 February 2015; accepted 28 April 2015
Published online 7 May 2015;
10.1126/science.aaa8720

CARBON CYCLE

The dominant role of semi-arid ecosystems in the trend and variability of the land CO_2 sink

Anders Ahlström,[1,2]* Michael R. Raupach,[3]† Guy Schurgers,[4] Benjamin Smith,[1] Almut Arneth,[5] Martin Jung,[6] Markus Reichstein,[6] Josep G. Canadell,[7] Pierre Friedlingstein,[8] Atul K. Jain,[9] Etsushi Kato,[10] Benjamin Poulter,[11] Stephen Sitch,[12] Benjamin D. Stocker,[13,14] Nicolas Viovy,[15] Ying Ping Wang,[16] Andy Wiltshire,[17] Sönke Zaehle,[6] Ning Zeng[18]

The growth rate of atmospheric carbon dioxide (CO_2) concentrations since industrialization is characterized by large interannual variability, mostly resulting from variability in CO_2 uptake by terrestrial ecosystems (typically termed carbon sink). However, the contributions of regional ecosystems to that variability are not well known. Using an ensemble of ecosystem and land-surface models and an empirical observation-based product of global gross primary production, we show that the mean sink, trend, and interannual variability in CO_2 uptake by terrestrial ecosystems are dominated by distinct biogeographic regions. Whereas the mean sink is dominated by highly productive lands (mainly tropical forests), the trend and interannual variability of the sink are dominated by semi-arid ecosystems whose carbon balance is strongly associated with circulation-driven variations in both precipitation and temperature.

Since the 1960s, terrestrial ecosystems have acted as a substantial sink for atmospheric CO_2, sequestering about one-quarter of anthropogenic emissions in an average year (*1*). This ecosystem service, which helps mitigate climate change by reducing the rate of increase of atmospheric greenhouse gases, is due to an imbalance between the uptake of CO_2 through gross primary production (GPP, the aggregate photosynthesis of plants) and the release of carbon to the atmosphere by ecosystem respiration (R_{eco}) and other losses, including wildfires (C_{fire}). The net carbon flux (net biome production, NBP = GPP − R_{eco} − C_{fire}) results from the small

Low-altitude magnetic field measurements by MESSENGER reveal Mercury's ancient crustal field

Catherine L. Johnson *et al.*

Science **348**, 892 (2015);
DOI: 10.1126/science.aaa8720